Available online at www.sciencedirect.com
SCIENCE DIRECT®
Journal of Sound and Vibration 290 (2006) 133–168
JOURNAL OF SOUND AND VIBRATION
www.elsevier.com/locate/jsvi

A wave model of a circular tyre. Part 2: side-wall and force transmission modelling

R.J. Pinnington*

Institute of Sound and Vibration Research, University of Southampton, Southampton SO17 1BJ, UK

Received 7 January 2004; received in revised form 11 February 2005; accepted 16 March 2005
Available online 14 July 2005

Abstract

A dynamic model of a curved side-wall of a pressurised tyre is presented. The model uses a previously derived wave equation. The side-wall is assumed to have a uniform thickness over the whole distance between the belt and the hub. A vertical or a horizontal displacement is input at the connection with the belt and the forces input and those transmitted to the hub are calculated and described in terms of dynamic stiffness. The effect of various parameters such as pressure, geometry, belt wavelength and material properties are investigated. The side-wall model is applied to a belt model to give a full tyre model. An integral around the belt circumference is performed to give the forces transmitted to the hub. The effect of the air within the cavity is calculated from the uncoupled carcass vibration. Finally, some experiments were made on a tyre and the model was fitted, thereby giving an estimate of the tyre material properties and validating the model for both belt vibration prediction and force transmission to the hub.

1. Introduction

A pneumatic tyre has two main components, the belt and the side-wall. The purpose of the belt is to provide a friction interface with the road, while the side-wall transmits traction, side forces and vehicle weight. Stiffening of the side-wall will therefore improve the vehicle handling but will transmit more road noise through the suspension to the passenger compartment. If a tyre is to be

*Corresponding author. Platia Skra 13, Kalamaria 55132, Thessaloniki, Greece. Tel./fax: +30 2310 480 645.
E-mail address: rjpinnington@compuserve.com.

0022-460X/$ - see front matter © 2005 Elsevier Ltd. All rights reserved.
doi:10.1016/j.jsv.2005.03.024

optimised for both vehicle handling and vibration transmission a model is needed for the side-wall that is valid for the complete frequency range of interest. For vehicle interior noise it is probably only necessary to have a model below 500 Hz. However, if there is also an intention to predict tyre surface vibration for sound radiation calculations this frequency range must be raised to around 3 kHz.

In the literature, the side-wall is usually represented as a simple stiffness, although in Refs. [1,2] this is associated with membrane forces controlled by the air-pressure and geometry. The only attempt at modelling the high-frequency dynamic effects of the side-wall are also found in Ref. [2], however, this model did not also extend down to the low-frequency region.

The objective here is therefore to make a wave model of a side-wall that will cover the complete frequency range of interest, i.e. 0–3 kHz. The outcome will be the dynamic stiffness/belt length in the radial, transverse and circumferential directions. This model is then applied to a belt model [3], from which surface vibration or transmitted forces can be provided.

At low frequencies the tyre stiffness derives from the balance of internal pressure and the angle that the side-wall tension makes with the belt or road surface [1,2]. At higher frequencies the side-wall bending stiffness, shear stiffness and longitudinal stiffness become important, and these are included in the model. The side-wall model presented here uses the same basic equations as the belt model [3], but with different boundary conditions. The least realistic feature is that it is assumed that the thickness is uniform over the length, while most side-walls are broad at the wheel hub and taper towards the line connection with the belt. No attempt is made to model the internal structure of the side-wall, and it is assumed that the average elastic moduli of the section are available.

In order to make force calculations to the hub, three other tasks are performed. The first is to modify the side-wall stiffness for a travelling wave input at the belt line input. The second is to find the integral of the transmitted force from the belt over the free belt length. The third is to find the force transmitted due to the acoustic waves within the cavity.

The model presented here is not quite complete as the air within the cavity is not included directly as a coupled equation of motion. The air-pressure is included as it controls the belt and side-wall tension. The calculation shows two air transmission mechanisms, one of which is responsible for the cavity resonance around 250 Hz that is detectable within the vehicle passenger compartment.

The side-wall model is combined with the belt model [3] to make a full tyre model, this model is fitted to some experimental data to give estimates of the material properties and the force transmitted to the hub. The measurements include two previously untried techniques for line excitation of the belt and for transmitted force to the hub.

2. Wave model of a curved side-wall

Fig. 1 shows a tyre side-wall of length l_s of radius a_s and uniform thickness t_s, displaying the sign convention for positive directions, rotations, forces and moments. It is assumed that the side-wall is symmetric about the neutral axis and that the averaged material properties of the cross-section are known. Reference will only be made to these single material values for the cross-section.

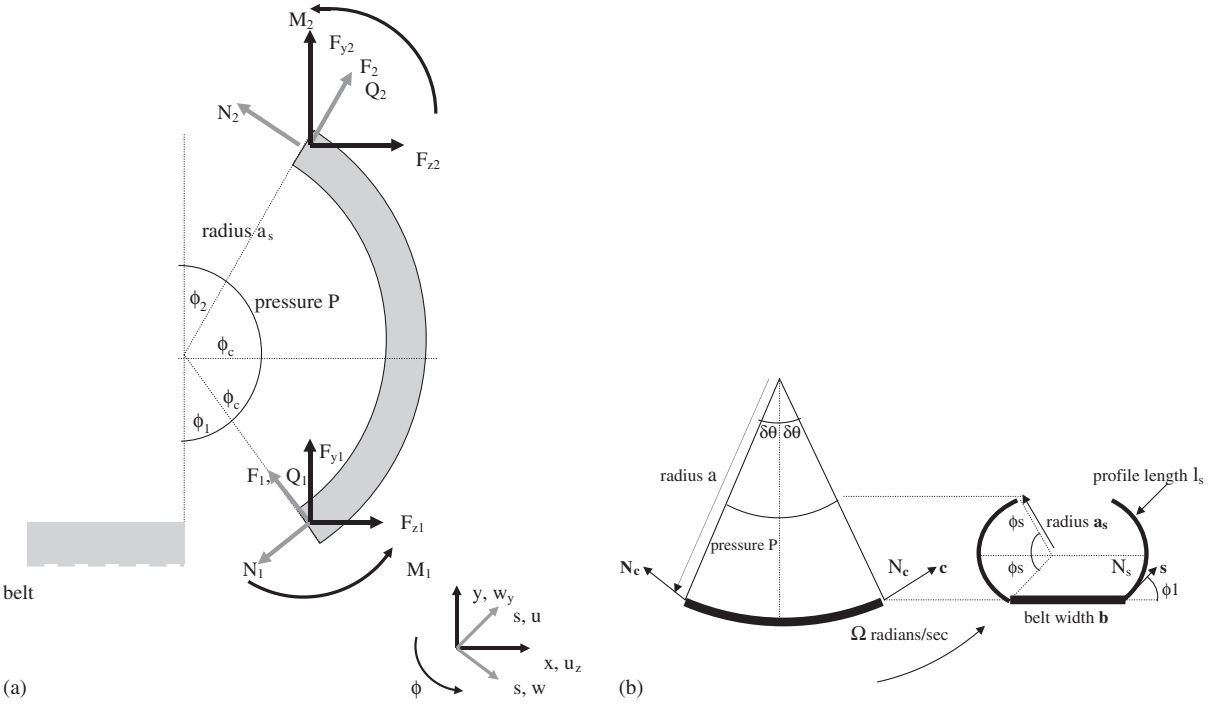

Fig. 1. Side-wall geometry: (a) single side-wall section and (b) belt and side-wall sections.

The side-wall is a curved, tensioned, Mindlin Plate (supporting bending and shear deformations) subjected to a net static pressure P. This pressure is balanced by a static tension/width N_s. Q_s is the shear force/width, N the total static and dynamic circumferencial force/width, M_s the bending/moment/width. The accompanying displacements are u, w, in the circumferential and radial directions. ϕ describes the geometric position, and is related to the arc coordinate s as $s = a_s\phi$. The kinematic rotation Φ_s includes contributions from both displacements u, w.

Vertical and horizontal displacements w_y, u_z are input from the connection with the belt at side-wall angle ϕ_1 from the vertical. At this position the distance coordinate $s = 0, s$ lies between 0 and l_s. The side-wall is symmetrical so that the radius a_s is given as

$$a_s = \frac{l_s}{\pi - \phi_1 - \phi_2} = \frac{l_s}{2\phi_s}. \tag{1}$$

The side-wall angle will be seen to have a large influence on the stiffness as it influences both the radius and the angle at which the static tension is applied to the hub and belt. The static tension is simply related to the pressure, $N_s = Pa_s$, if the side-wall assumes the arc of a circle.

The other four boundary conditions that are assumed here (although others could be used), are at $s = 0$ the bending moment is assumed to be zero as the side-wall tapers here. Between the hub and the stiff wire tyre beading a layer of rubber forms a seal. Perhaps the best model of this junction would be a rotational stiffness that would allow any possibility between the simple supported and clamped conditions. However, for simplicity the stiffer extreme was selected so that

at $s = l_s$ the displacements and slope due to bending are set to zero. This choice will have a slight effect on the stiffness although it will be seen that the tension is the dominant effect which does not depend on the rotational boundary conditions.

The input displacements cause input forces F_{y1}, F_{z1} and transmitted forces F_{y2}, F_{z2}. These forces when normalised by the displacements provide the required input and transfer dynamic stiffness'.

2.1. The wave equation

The wave equation is a modified version of Eq. (31) in Ref. [3]. The coordinate s in the arc direction of the side-wall replaces the corresponding belt coordinate c in all the material and geometric constants, i.e.

$$\begin{aligned} 0 = {} & z^6(\bar{S}_s + \bar{N}_s) \\ & - z^4[z_{Ls}^2 + \bar{P}a_s - \bar{N}_s\bar{R}_s + (\bar{S}_s + \bar{N}_s)(1 + z_s^2 + z_{Ls}^2)] \\ & + z^2[(-z_{Ls}^2)(1 - \bar{P}a_s - \bar{S}_s - z_{Ls}^2 + \bar{N}_s\bar{R}_s - z_s^2(\bar{S}_s + \bar{N}_s)) + (z_s^2 - \bar{R}_s)(\bar{N}_s + \bar{P}a_s + z_{Ls}^2)] \\ & + (1 - \bar{P}a_s - z_{Ls}^2)(z_s^2 - \bar{R}_s)(z_{Ls}^2). \end{aligned} \tag{2}$$

The non-dimensional constants are:

$$\bar{S}_s = \frac{S_s}{A_s}, \quad \bar{N}_s = \frac{N_s}{A_s}, \quad \bar{P}a_s = \frac{Pa_s}{A_s}, \quad \bar{R}_s = a_s^2\frac{S_s}{B_s},$$

S_s, A_s are the shear stiffness/length and longitudinal stiffness/length. N_s, B_s are the in-plane force/length and bending stiffness/length. The normalised wavenumber z is ka_s. The normalised non-dimensional longitudinal wavenumber z_{Ls} is defined by

$$z_{Ls}^2 = (a_s\omega)^2\frac{\mu_s}{A_s}.$$

There is also a wave that cuts on at high frequencies that involves only section rotation and no translation, here it is called the 'rotational wave'. The wavenumber z_s is defined by

$$z_s^2 = (a_s\omega)^2\frac{I_s}{B_s},$$

where μ_s, I_s are the side-wall mass/area and rotational inertia/area, $I_s = \mu t_s^2/12$.

2.2. The wavenumbers and displacement amplitude ratios

A standard set of parameters in Table 1 was applied to the wave equation. The three roots of waves in the positive s direction were found from a MATLAB programme. The modulus and phase of the wavenumbers were found and are displayed in Figs. 2a, b. The associated ratio of longitudinal/transverse motion, u/w, are given in Fig. 2c to aid the interpretation, the basis of which is given in Ref. [3]. The line labelled dominant belt real wavenumber is discussed in Section 3.3.

Table 1
Side-wall parameters

Parameters	Symbol	Size equation	Units
Internal pressure	P	2×10^5	N/m^2
Side-wall thickness	t_s	0.7×10^{-2}	m
Side-wall radius	a_s	0.3	m
Side-wall angle	θ_s	$\pi/6$	rad
Tensile force/width	N_s	$P \times a_s$	N/m
Shear modulus	G_s	3×10^6	N/m^2
Shear stiffness/width	S_s	$G_s \times t_s$	N/m
Bending stiffness/width	B_s	$G_s \times t_s^3/4$	Nm
Axial stiffness/width	A_s	4.7×10^5	N/m
Belt mass/area	μ_s	7.7	kg/m^2
Rotational inertia/width	I_s	$\mu_s \times \mu_s^2/12$	kg
Rotational and shear loss factor	η_1	0.15	
Axial and tension loss factor	η_2	0.1	

2.2.1. Wavenumber root 1

In Fig. 2a, the magnitude of root 1 is seen as a constant at a value that gives $ka_s = \pi/2$ until 100 Hz. The ratio of u/w in Fig. 2c is about $\frac{2}{3}$. These three characteristics describe the changing shape of an in-elastic side-wall that bulges as the belt moves towards the hub, which is the dominant mechanism of load support.

At higher frequencies the wavenumber magnitude increases in proportion to frequency, the small negative phase angle and small u/w ratio suggests a tension-dominated travelling wave. If the internal pressure was removed and hence the tension, this wave would be controlled by the bending stiffness. At very high frequencies above 3 kHz this wave is controlled by the shear stiffness.

2.2.2. Wavenumber root 2

Fig. 2c indicates that this is a longitudinal wave. Below the side-wall ring frequency at 400 Hz the phase of $-\pi/2$ implies an evanescent wave. At 400 Hz the rapid phase change marks the ring frequency, above which a longitudinal travelling wave occurs. This wave is controlled by the side-wall longitudinal stiffness.

2.2.3. Wavenumber root 3

The third root has a phase of $-\pi/2$ until the cut-on of the rotational travelling wave at 4 kHz. This means that it is an evanescent wave below this frequency. The large wavenumber implies rapid decay of vibration away from the belt towards the hub.

2.3. The transfer functions

Fig. 1 is a display of the side-wall subjected to displacements at the belt contact ϕ_1. If a lateral displacement u_{z1} or a vertical displacement w_{y1} is applied to the side-wall it causes responses at

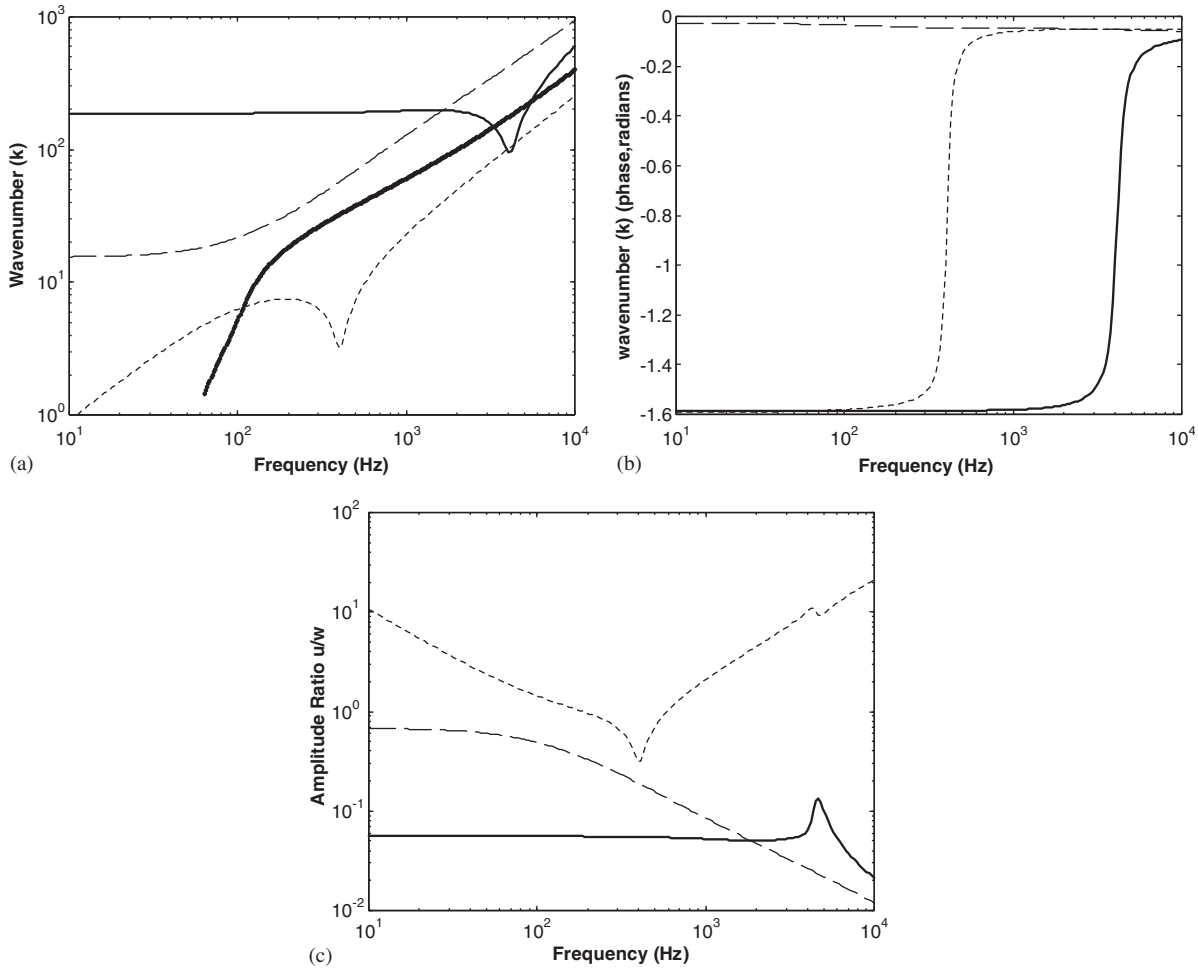

Fig. 2. Wavenumber (a) modulus; ––– root 1, - - - root 2, — root 3, —— top belt root; (b) phase and (c) wave amplitude ratio: – – – root 1, - - - root 2, — root 3.

every point s, in both the circumferencial u and radial w directions. The force responses at $s = 0$ and l_s are quantified in the 'dynamic stiffness' transfer function, which is force/displacement. The dynamic stiffness' can be calculated from the summation of the three pairs of waves that exist at each frequency. The amplitudes of these waves are found from the six boundary conditions at the contact line with the hub and with the belt.

A matrix of lateral wave amplitudes is written. These are used to give slopes Φ, in-plane displacements, shear rotation γ, bending rotation β, in-plane forces N, shear forces Q and moments M. The six boundary conditions are then expressed as a matrix in terms of the lateral displacements. The solution of this matrix gives the wave amplitudes and hence the transfer functions.

2.3.1. Transverse displacement

The wavenumbers for the three wave pairs obtained from the wave equation are, $k_{pa}, k_{pb}, p = 1, 2, 3$; a (anti-clockwise), b (clockwise), denote the direction of the wave propagation. $k_{pa} = k_{pb} = k_p$ for all waves as there is no rotation of the side-wall in the circumferential direction. The transverse amplitudes of each of the three pairs of waves; w_{pa}, w_{pb}, are given in a column matrix $\mathbf{w}_p$

$$\mathbf{w}_p = \begin{Bmatrix} w_{1a} \\ w_{1b} \\ w_{2a} \\ w_{2b} \\ w_{3a} \\ w_{3b} \end{Bmatrix}. \tag{3}$$

At position s each wave becomes phase-lagged and attenuated in accordance with the 6×6 diagonal matrix $\mathbf{L}_{ps}$

$$\mathbf{L}_{ps} = \mathrm{diag}[\mathrm{e}^{-\mathrm{i}k_1 s}, \alpha_1 \mathrm{e}^{\mathrm{i}k_1 s}, \mathrm{e}^{-\mathrm{i}k_2 s}, \alpha_2 \mathrm{e}^{\mathrm{i}k_2 s}, \mathrm{e}^{-\mathrm{i}k_3 s}, \alpha_3 \mathrm{e}^{\mathrm{i}k_3 s}], \tag{4}$$

where the exponential attenuation and phase-lag over the side-wall length $l_s = 2\phi_s a_s$ is

$$\alpha_p = \exp(-\mathrm{i}k_p l_s).$$

The column matrix for weighted wave amplitude and phase is $\mathbf{w}_{ps}$

$$\mathbf{w}_{ps} = \mathbf{L}_{ps}\mathbf{w}_p. \tag{5}$$

The transverse displacement $w(s)$ at any point s is the sum of the six waves in Eq. (5)

$$w(s) = \mathbf{I}^{\mathrm{T}}\mathbf{w}_{ps}, \tag{6}$$

where the row matrix $\mathbf{I}^{\mathrm{T}} = \{1\ \ 1\ \ 1\ \ 1\ \ 1\ \ 1\}$ is just a device to make the sum.

The slope at any point s is obtained using the differential operator $\mathbf{D}_p$

$$\frac{\partial w}{\partial s} = \mathbf{I}^{\mathrm{T}}\mathbf{D}_p\mathbf{w}_{ps}, \tag{7}$$

where $\mathbf{D}_p = \mathrm{diag}[-\mathrm{i}k_1, \mathrm{i}k_1, -\mathrm{i}k_2, \mathrm{i}k_2, -\mathrm{i}k_3, \mathrm{i}k_3]$.

2.3.2. Longitudinal displacement

The longitudinal displacement u_p is the transverse displacement w_p weighted by the displacement ratios A_p, for anti-clockwise and clockwise pth waves

$$u_p = A_p w_p. \tag{8a,b}$$

The displacement ratios for the anti-clockwise and clockwise waves is found by substituting the harmonic travelling wave solutions $\exp(\mp \mathrm{i}k_p s)$ into Eq. (29), [3], to give for the anti-clockwise wave

$$A_p = \frac{-\mathrm{i}z_p}{z_p^2 - z_{Ls}^2}, \quad p = 1, 2, 3. \tag{9a,b}$$

The clockwise wave has the opposite sign. The total longitudinal displacement $u(s)$ is the sum of the six wave displacements $\mathbf{u}_p$, given from Eq. (5)

$$u(s) = \mathbf{I}^{\mathrm{T}}\mathbf{A}_p\mathbf{w}_{ps}. \tag{10}$$

The diagonal matrix of displacement ratios is

$$\mathbf{A}_p = \mathrm{diag}[A_1, -A_1, A_2, -A_2, A_3, -A_3].$$

2.3.3. The slope due to bending

The gradient $\partial w/\partial s$ is given in Eq. (1) [3], as the sum of the bending slope β and the shear γ. The slope due to bending is related to the gradient by Eq. (14a) [3]. On substitution of the harmonic solution for a clockwise or anti-clockwise travelling wave p, and using the normalisation of Eq. (26), [3]

$$\beta_p = E_p \frac{\partial w_p}{\partial s}, \tag{11}$$

where

$$E_p = \frac{1 + \bar{R}_s}{z_p^2 - z_s^2 + \bar{R}_s}.$$

The diagonal matrix of wave weighting functions, $\mathbf{E}_p$ is

$$\mathbf{E}_p = \mathrm{diag}[E_1, E_1, E_2, E_2, E_3, E_3]. \tag{12}$$

2.4. The boundary conditions

There are six boundary conditions, three at each end of the side-wall. All the boundary conditions are expressed in terms of the six transverse wave amplitudes $\mathbf{w}_p$. As the boundary conditions are initially in radial coordinates they must be transformed into Cartesian coordinates using a transformation matrix. At $s = 0$, the displacements are:

$$\begin{Bmatrix} w_1 \\ u_1 \end{Bmatrix} = \boldsymbol{\phi}_1 \begin{Bmatrix} w_{y1} \\ u_{z1} \end{Bmatrix}; \quad \boldsymbol{\phi}_1 = \boldsymbol{\phi}_1^{-1} = \begin{bmatrix} -\cos\phi_1 & \sin\phi_1 \\ \sin\phi_1 & \cos\phi_1 \end{bmatrix}. \tag{13}$$

The forces at $s = 0$ are:

$$\begin{Bmatrix} F_{y1} \\ F_{z1} \end{Bmatrix} = -\boldsymbol{\phi}_1 \begin{Bmatrix} F_1 \\ N_1 \end{Bmatrix}. \tag{14}$$

The forces at $s = l_s$ are:

$$\begin{Bmatrix} F_{y2} \\ F_{z2} \end{Bmatrix} = \boldsymbol{\phi}_2 \begin{Bmatrix} F_2 \\ N_2 \end{Bmatrix}; \quad \boldsymbol{\phi}_2 = \begin{bmatrix} \cos\phi_2 & \sin\phi_2 \\ \sin\phi_2 & -\cos\phi_2 \end{bmatrix}. \tag{15}$$

2.4.1. Radial displacement at $s = 0$

The radial displacement w_1 is given in Eq. (13) from the input displacements, and from Eq. (5), setting $s = 0$

$$w_1 = \mathbf{I}^{\mathrm{T}}\mathbf{L}_{ps}(0)\mathbf{w}_p \tag{16}$$

and by expanding the matrices

$$w_1 = \mathbf{B}_{1p}\mathbf{w}_p,$$

where

$$\mathbf{B}_{1p} = [1 \quad \alpha_1 \quad 1 \quad \alpha_2 \quad 1 \quad \alpha_3].$$

2.4.2. Circumferential displacement at $s = 0$

The longitudinal displacement u_1 is given in Eq. (13) from the input displacements, and from Eq. (10), setting $s = 0$

$$u_1 = \mathbf{I}^{\mathrm{T}}\mathbf{A}_p\mathbf{L}_{ps}(0)\mathbf{w}_p \tag{17}$$

and by expanding the matrices

$$u_1 = \mathbf{B}_{2p}\mathbf{w}_p,$$

where

$$\mathbf{B}_{2p} = [A_1 \quad -\alpha_1 A_1 \quad A_2 \quad -\alpha_2 A_2 \quad A_3 \quad -\alpha_3 A_3].$$

2.4.3. Bending moment at $s = 0$

The bending moment is assumed to be zero in this case, although it is possible to insert a rotational stiffness instead. However, for the zero moment it can be said that the gradient in the bending slope is zero

$$\frac{\partial\beta(0)}{\partial s} = 0.$$

Eqs. (7) and (11) relate this to the radial displacements

$$0 = \mathbf{I}^{\mathrm{T}}\mathbf{E}_p\mathbf{D}_p^2\mathbf{L}_{ps}(0)\mathbf{w}_p. \tag{18}$$

On expanding the matrices

$$0 = \mathbf{B}_{3p}\mathbf{w}_p,$$

where

$$\mathbf{B}_{3p} = [-k_p^2 E_p \quad -k_p^2\alpha_p E_p \ldots\ldots\ldots\ldots\ldots\ldots\ldots\ldots\ldots], \quad p = 1, 2, 3.$$

2.4.4. Slope from bending at $s = l_s$

The slope from bending is zero in this case as a clamped termination is assumed. Although as above, it is possible to insert a rotational stiffness instead. For zero bending slope

$$\beta(l_s) = 0. \tag{19}$$

With Eqs. (7) and (11) this can be related to the radial displacements, setting $s = l_s$

$$0 = \mathbf{I}^{\mathrm{T}}\mathbf{E}_p\mathbf{D}_p\mathbf{L}_{ps}(l_s)\mathbf{w}_p \tag{20}$$

and by expanding the matrices

$$0 = \mathbf{B}_{4p}\mathbf{w}_p,$$

where

$$\mathbf{B}_{4p} = [-\mathrm{i}k_p\alpha_p E_p \quad \mathrm{i}k_p E_p \ldots\ldots\ldots\ldots\ldots\ldots\ldots\ldots\ldots], \quad p = 1, 2, 3.$$

2.4.5. Radial displacement at $s = l_s$

The radial displacement w_1 is zero for the clamped boundary, and from Eq. (5)

$$0 = \mathbf{I}^{\mathrm{T}}\mathbf{L}_{ps}(l_s)\mathbf{w}_p \tag{21}$$

and by expanding the matrices

$$0 = \mathbf{B}_{5p}\mathbf{w}_p,$$

where

$$\mathbf{B}_{5p} = [\alpha_1 \quad 1 \quad \alpha_2 \quad 1 \quad \alpha_3 \quad 1].$$

2.4.6. Circumferential displacement at $s = l_s$

The longitudinal displacement is zero for the clamped boundary, and from Eq. (10)

$$0 = \mathbf{I}^{\mathrm{T}}\mathbf{A}_p\mathbf{L}_{ps}(l_s)\mathbf{w}_p \tag{22}$$

and by expanding the matrices

$$0 = \mathbf{B}_{6p}\mathbf{w}_p,$$

where

$$\mathbf{B}_{6p} = [\alpha_1 A_1 \quad -A_1 \quad \alpha_2 A_2 \quad -A_2 \quad \alpha_3 A_3 \quad -A_3].$$

2.5. Assembly of dynamic stiffness matrices

The six boundary conditions from Eqs. (16) to (22) can now be assembled into a single matrix

$$\mathbf{B}_p\mathbf{w}_p = \mathbf{w}, \quad \mathbf{B}_p = \begin{bmatrix} \mathbf{B}_{1p} \\ \mathbf{B}_{2p} \\ \mathbf{B}_{3p} \\ \mathbf{B}_{4p} \\ \mathbf{B}_{5p} \\ \mathbf{B}_{6p} \end{bmatrix}, \quad \mathbf{w} = \begin{Bmatrix} w_1 \\ u_1 \\ 0 \\ 0 \\ 0 \\ 0 \end{Bmatrix}. \tag{23}$$

This may be inverted to give the wave amplitudes

$$\mathbf{w}_p = \mathbf{B}_p^{-1}\mathbf{w}. \tag{24}$$

2.5.1. The transverse and longitudinal forces

The net transverse force/width F in the radial direction in Fig. 1 has contributions from the component internal shear forces/width Q_{s1} and tension forces/width N at $s = 0$ or $s = l_s$

$$F_1 = [Q_{s1} - N_1\Phi_s]_{s=0}, \tag{25a}$$

$$F_2 = [Q_{s2} - N_2\Phi_s]_{s=l_S}. \tag{25b}$$

The kinematic rotation Φ_s, is given in Eq. (2), [1]

$$\Phi_s = \frac{u}{a_s} - \frac{\partial w}{\partial s}. \tag{26}$$

The shear force for the pth wave is the product of shear stiffness S_s and shear slope γ and can be written in terms of w_p using Eqs. (1), (8) and (44) of Ref. [3]

$$Q_p = S_s(1 - E_p)\frac{\partial w_p}{\partial s}. \tag{27}$$

If only the static in-plane force is considered, i.e. $N = N_s$, then substitution into Eq. (25) of Eqs. (4), (7), (10), (11), (26) and (27), yield the net transverse force F at s

$$F = \mathbf{I}^{\mathrm{T}}\left((S_s + N_s)\mathbf{D}_p - S_s\mathbf{E}_p\mathbf{D}_p - \frac{N_s}{a_s}\mathbf{A}_p\right)\mathbf{L}_{ps}\mathbf{w}_p. \tag{28}$$

The longitudinal forces N, in Fig. 1, are simply the product of the longitudinal stiffness A_s and the longitudinal strain

$$N = A_s\left(\frac{\partial u}{\partial s} + \frac{w}{a_s}\right). \tag{29}$$

This can be written in terms of $\mathbf{w}_p$ using Eqs. (4), (7) and (10)

$$N = -A_s\mathbf{I}^{\mathrm{T}}\left(\mathbf{D}_p\mathbf{A}_p + \frac{1}{a_s}\mathbf{I}_0\right)\mathbf{L}_{ps}\mathbf{w}_p, \tag{30}$$

where $\mathbf{I}_0$ is the unit matrix. The radial and longitudinal forces in Eqs. (28) and (30) can be written in a single stiffness matrix $\mathbf{K}_p$

$$\mathbf{F}_s = \begin{Bmatrix} F \\ N \end{Bmatrix} = \mathbf{K}_p\mathbf{L}_{ps}\mathbf{w}_p, \tag{31}$$

where the stiffness matrix is

$$\mathbf{K}_p = [\mathbf{K}_{1a} \quad \mathbf{K}_{1b} \quad \mathbf{K}_{2a} \quad \mathbf{K}_{2b} \quad \mathbf{K}_{3a} \quad \mathbf{K}_{3b}], \tag{32}$$

$$[\mathbf{K}_{pa} \quad \mathbf{K}_{pb}] = \begin{bmatrix} \left\{ \mathrm{i}k_p(S_s(1-E_p)+N_s) - \dfrac{N_s}{a_s}A_p \right\} & \left\{ \mathrm{i}k_p(S_s(1-E_p)+N_s) + \dfrac{N_s}{a_s}A_p \right\} \\ A_s\left(-\mathrm{i}k_pA_p + \dfrac{1}{a_s}\right) & A_s\left(-\mathrm{i}k_pA_p + \dfrac{1}{a_s}\right) \end{bmatrix}, \quad p = 1,2,3.$$

The vertical force and horizontal force at $s = 0$ can now be written using the transformation matrix in Eq. (13)

$$\begin{Bmatrix} F_{y1} \\ N_{z1} \end{Bmatrix} = -\boldsymbol{\phi}_1 \mathbf{K}_p \mathbf{L}_{ps}(0)\mathbf{w}_p. \tag{33}$$

Likewise the vertical force and horizontal force at $s = l_s$ can now be written using the transformation matrix in Eq. (14):

$$\begin{Bmatrix} F_{y2} \\ N_{z2} \end{Bmatrix} = \boldsymbol{\phi}_2 \mathbf{K}_p \mathbf{L}_{ps}(l_s)\mathbf{w}_p. \tag{34}$$

The wave amplitudes $\mathbf{w}_p$ are given in Eqs. (23), (24) as a function of input displacements w_1, u_1.

2.5.2. *Vertical dynamic stiffness'*

The vertical input and transfer dynamic stiffness' are given from F_{y1}, F_{y2} by setting $w_1 = 1, u_1 = 0$.

2.5.3. *Horizontal dynamic stiffness'*

The horizontal input and transfer dynamic stiffness' are given from F_{z1}, F_{z2} by setting $w_1 = 0, u_1 = 1$.

2.6. *Parameter study on two-dimensional side-wall dynamic stiffness'*

Eqs. (33) and (34) are applied for various parameter changes with the values in Table 1 taken as the norm. These include excitation direction, internal pressure P, the angle subtended by the side-wall ϕ_s, and side-wall angle thickness t_s. The main purpose here is to consider the static and low-frequency stiffness' in the vertical and lateral directions, which is most important for vehicle handling and whole body vehicle motion.

2.6.1. *Side-wall stiffness for vertical excitation*

Fig. 3 shows the vertical side-wall stiffness/length for a vertical displacement applied at the tyre/road interface. Below 220 Hz the side-wall behaves as a static stiffness of about $1.5 \times 10^6\,\mathrm{N/m^2}$, which is slightly lower than the value of $2 \times 10^6\,\mathrm{N/m^2}$ obtained from the expression for an inelastic side-wall [2]. The discrepancy almost certainly arises from the fact that the side-wall can in fact stretch and has an in-plane stiffness of $4.5 \times 10^6\,\mathrm{N/m^2}$, as seen in Fig. 7. At 220 Hz a dip occurs corresponding to a resonance of the side-wall if excited by a force at the road. There are then a series of sharp peaks, the lowest near 400 Hz, the ring frequency. Above the ring frequency the peaks and mean slope are associated with the in-plane motion of the side-wall, i.e. the

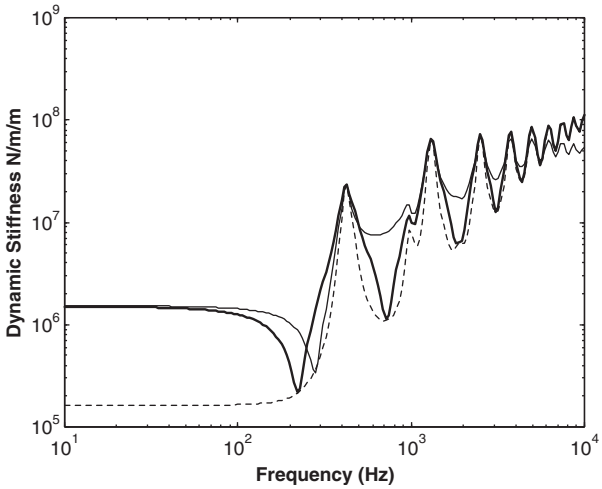

Fig. 3. Vertical dynamic stiffness/length: - - - input real part, — transfer modulus, —— input modulus.

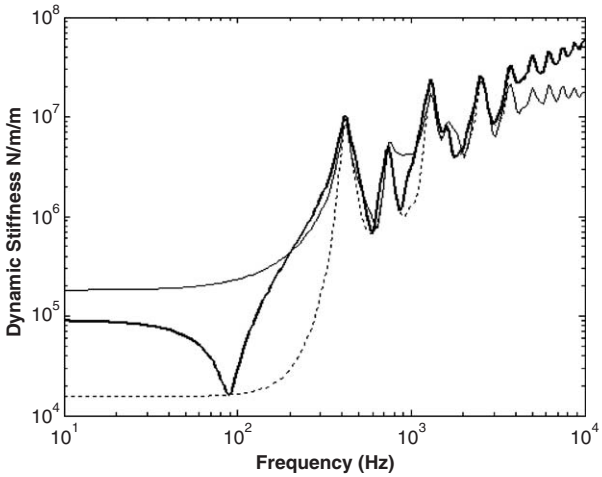

Fig. 4. Horizontal dynamic stiffness/length: - - - input real part, — transfer modulus, —— input modulus.

behaviour could be modelled as a plate excited in-plane [2]. The transfer stiffness and input stiffness are similar except at the troughs.

2.6.2. Side-wall stiffness for horizontal excitation

The lateral stiffness is shown in Fig. 4. The static value, below 20 Hz is about a twentieth of the vertical value seen in Fig. 3. This shows the shortcoming of pneumatic tyres, as lateral stiffness is desirable for sharp vehicle handling but vertical stiffness only serves to transmit road noise.

The stiffness characteristic at higher frequencies is similar to the vertical excitation case, with the in-plane motion dominant. In this frequency range, the side-wall is stiffer in the vertical direction than the horizontal direction by a factor between two and three, as would be expected

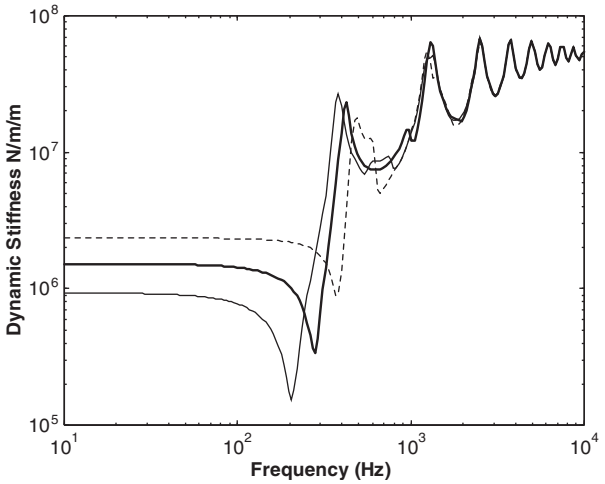

Fig. 5. Vertical dynamic stiffness/length vs. pressure: — 1 bar, —— 2 bar, - - - 4 bar.

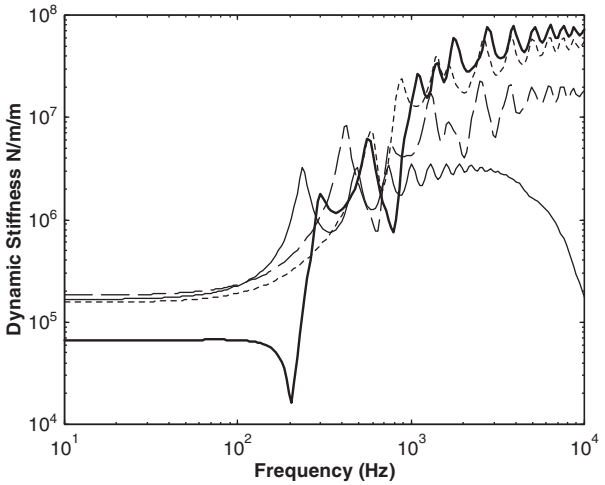

Fig. 6. Horizontal transfer stiffness modulus/length vs. side-wall angle: —— 0 rad, - - - $\pi/6$ rad, – – – $\pi/3$ rad, — $\pi/2$ rad.

from the angle of the side-wall to the horizontal, i.e.

$$\cos^2(\phi_s)/\sin^2(\phi_s) = 3, \quad \phi_s = \pi/6.$$

2.6.3. The effect of inflation pressure

Fig. 5 shows the transfer stiffness to the hub from the road for various inflation pressures. The norm is 2 bar which lies in the centre. If the pressure P is raised or lowered by a factor of two the frequency stiffness changes accordingly. This is expected as the in-plane tension N_s is responsible for the static stiffness, and this is proportional to the pressure. $N_s = Pa_s$, where a_s is

the side-wall radius. Above the ring frequency at 400 Hz the pressure has little influence as the longitudinal stiffness is the dominant factor.

2.6.4. The effect of the angle of the side-wall, transverse excitation and vertical excitation

In Fig. 6 the angle that is subtended by the side-wall ϕ_s is varied between 0 (vertical profile) and $\pi/2$ (semicircular profile). The length of the side-wall profile is maintained constant. The angle has little effect on the static transverse stiffness until it softens as the angle approaches 0°. At this position the side-wall behaves as a straight tensioned beam.

The trend is reversed for vertical excitation, seen in Fig. 7. The side-wall is stiffest when the subtended angle is 0°, as it behaves as a plate driven in-plane. The softest value occurs when the side-wall profile is semicircular when the angle is $\pi/2$. On this superficial basis it would appear

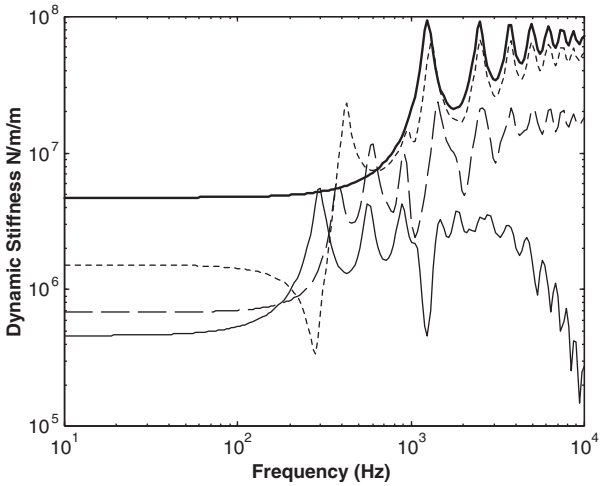

Fig. 7. Vertical transfer stiffness modulus/length vs. side-wall angle: —— 0 rad, - - - $\pi/6$ rad, – – – $\pi/3$ rad, — $\pi/2$ rad.

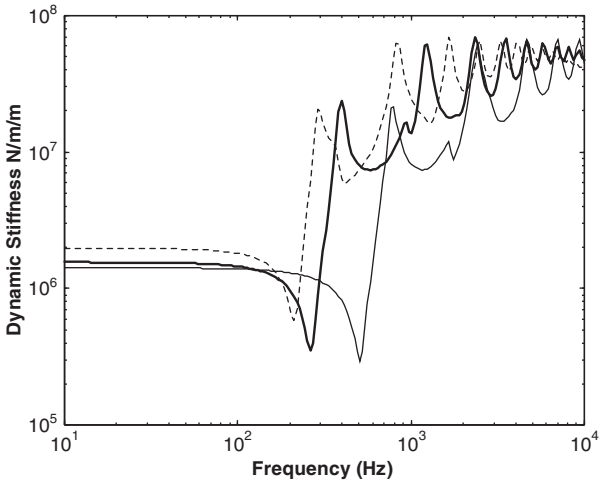

Fig. 8. Vertical transfer stiffness modulus/length vs. side-wall thickness: —— 8 mm, - - - 16 mm, — 2 mm.

that maximising lateral stiffness and minimising vertical stiffness is achieved with the semicircular profile. The vertical stiffness in this case is only three times greater than the horizontal stiffness, as opposed to a factor of 20 of the standard case.

2.6.5. The effect of side-wall thickness

The side-wall can be regarded as an elastomer plate with nylon cords aligned approximately in the radial direction to resist the pressure. An increase in wall thickness increases the weight and bending stiffness but has little bearing on the tension forces and in-plane elastic forces. Accordingly, Fig. 8 shows that apart from a slight increase in static stiffness the main effect of increasing the thickness is to lower the natural frequencies and hence degrade the performance over the whole frequency range.

3. The side-wall stiffness when excited by a travelling wave

In the previous section it was implied that the side-wall was excited in-phase over the length. However, on a real tyre it is the in-plane and transverse wave motion of the belt that drives the side-wall boundary. It is therefore necessary to modify the previous stiffness' for the case of a side-wall (or plate) excited by a wave at the boundary. Nevertheless this modification will have no effect on the static stiffness' discussed in the previous section, only on the characteristics above the first side-wall resonance.

The example here will only include one wavetype and the shear waves generated by the belt circumferential or longitudinal motion are chosen, being the most simple, described by a second-order differential equation. It will be shown that the effects depend upon the relative sizes of the side-wall (or plate), free wavenumber and the excitation wavenumber from the belt at the boundary.

3.1. Complex wavenumbers normal to the boundaries

Fig. 9 shows an infinite orthogonal plate strip of width l_y, representing the side-wall. The wavenumber k_y, across a strip of width l_y, is very similar to that of the one-dimensional system of the same length, considered previously. However, for the strip, the wavenumber k_y has a larger attenuation part due to the extra distance actually travelled between boundaries by the non-normal wave front. Two methods of finding this damped wavenumber in the y direction are obtained by considering the in-plane response of the strip to an inexorable x displacement $U_0 \exp(-\mathrm{i}k_x x)$, travelling in the x direction at the boundary $y = 0$. The in-plane wave was selected as it is the simplest description of the physics.

The plate has different free wavenumbers in the orthogonal directions x, y

$$\bar{k}_x = k_x - \mathrm{i}k'_x,$$

$$\bar{k}_y = k_y - \mathrm{i}k'_y. \tag{35a,b}$$

Take for example, the x direction wavenumber. The real part is positive, describing the changing phase of a wave progressing in the x direction. The imaginary part is negative, indicating the

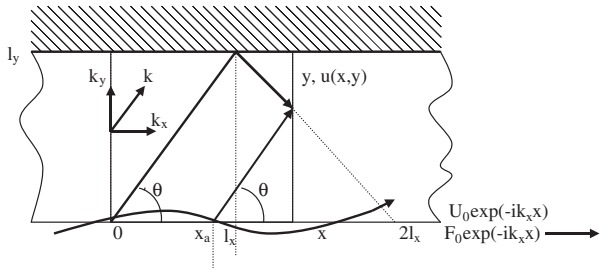

Fig. 9. Edge excited plate strip.

attenuation of the wave travelling in the x direction. The real component of the wavenumber in the x direction k_x, must correspond to the wavenumber of the imposed displacement at the boundary at $y = 0$. The y wavenumber component $\bar{k}_y$ describes a free wave which satisfies the boundary conditions at both $y = 0$ and l_y.

The imposed displacement causes a shear force $F_0 \exp(-\mathrm{i}k_x x)$ at $y = 0$ and a transmitted shear force to the rigid boundary at $y = l_y$. The displacement at any point (x, y) for $x > l_x$ is the sum of two plane waves, an incident plane wave coming directly through point $(x_a, 0)$, another reflected wave comes through $(0, 0)$ via the other boundary at (l_x, l_y). The phase of these waves depends only on the x, y coordinates, but the amplitudes depend on the attenuation in the medium of the two paths shown. The incident wave travels a distance in the x direction

$$x - x_a = y \cot \theta. \tag{36a}$$

The reflected wave travels a distance in the x direction of

$$x = 2l_x - y \cot \theta, \tag{36b}$$

where $l_x = l_y \cot \theta$. Then Eq. (36b) can be written as $x = (2l_y - y) \cot \theta$. The incident wave begins with amplitude A at the origin, and travels on the boundary without attenuation, and real wavenumber k_x, until x_a when it enters the medium to be attenuated until the observation point x, y. The reflected wave also leaves the origin with amplitude A but travels with attenuation through the medium and suffers one reflection at $y = l_y$, with reflection coefficient $\hat{r}$. These two waves can be summed below to give the displacement at point x, y. The first term is the incident wave and the second term is the reflected wave.

$$u(x, y) = A\{\exp(-\mathrm{i}\hat{k}_y y) + \hat{r}\hat{\alpha}_y^2 \exp(\mathrm{i}\hat{k}_y y)\} \exp(-\mathrm{i}k_x x). \tag{37a}$$

This is now an equation for one-dimensional waves in the y direction; the complex wavenumber is the same as before but now with extra attenuation dependent upon the angle of incidence to the boundary θ

$$\hat{k}_y = \bar{k}_y - \mathrm{i}k'_x \cot \theta. \tag{37b}$$

For normal incidence there is no extra attenuation, while for grazing incidence the attention becomes infinite because of the increased path, i.e. l_x becomes infinite. $\hat{\alpha}_y$ is the attenuation and

phase change as the wave between the boundaries separated by distance l_y

$$\hat{\alpha}_y = \exp(-\mathrm{i}\hat{k}_y l_y). \tag{37c}$$

The complex wavenumber $\hat{k}_y$ can actually be found much more directly, but without physical interpretation from the vector summation of wavenumbers seen in Fig. 9

$$\hat{k}_y = \sqrt{\bar{k}^2 - k_x^2}, \quad \bar{k}^2 = \bar{k}_x^2 + \bar{k}_y^2. \tag{38a,b}$$

The real and complex wavenumbers are defined in Eq. (35). It is to be noted that the purely real wavenumber k_x imposed on the boundary is used in Eq. (38a). If the loss factor η, in directions x and y are the same, then Eq. (38b) becomes

$$\bar{k}^2 = \frac{k_x^2 + k_y^2}{1 + \mathrm{i}\eta}. \tag{38c}$$

By making this substitution into Eq. (38a) the modified wavenumber in the y direction is

$$\hat{k}_y = \frac{k_y}{\sqrt{1+\eta^2}} \sqrt{1 - (\eta \cot\theta)^2 - \mathrm{i}\eta(1 + \cot\theta)^2}, \quad \cot\theta = \frac{k_x}{k_y}. \tag{39}$$

This is the alternative form of the modified wavenumber seen in Eq. (37). Eq. (38) or (39) is more useful than Eq. (37) as it is applicable to any level of damping and any wavenumber combination.

3.1.1. Travelling wave propagation ($k > k_x$) and light damping ($\eta \ll 1$)

If $k > k_x$ a travelling wave is radiated into the plate by the edge excitation. If there is also light damping ($\eta \ll 1$), Eq. (39) reduces to

$$\hat{k}_y = k_y \left(1 - \frac{\mathrm{i}\eta}{2} - \mathrm{i}\frac{\eta k_x}{2}\cot\theta\right) \tag{40}$$

showing increasing attenuation with angle of incidence, identical to Eq. (35).

3.1.2. Coincidence between the excitation and plate wavenumbers ($k = k_x$)

If there is light damping and there is matching of the excitation and the plate wavenumber in the x direction ($k = k_x$), Eq. (39) becomes

$$\hat{k}_y = \pm k(1 - \mathrm{i})\sqrt{\frac{\eta}{2(1+\eta^2)}}. \tag{41}$$

This represents an evanescent wave normal to the boundary if the positive root is selected.

3.1.3. Above coincidence between the excitation and the plate ($k_x \gg k$)

If the excitation wavenumber is greater than the plate wavenumber, waves cannot propagate away from the boundary, and Eq. (39) becomes mainly imaginary as for an evanescent wave

$$\hat{k}_y = -\mathrm{i}k_x + \eta\left(\frac{k}{k_x}\right)^2 \frac{k_x}{1+\eta^2}. \tag{42}$$

3.1.4. Boundary wave that is evanescent

If the excitation is an evanescent wave of the form $U_0 \exp(-k_x x)$, the excitation wavenumber becomes purely imaginary and so Eq. (38a) becomes

$$\hat{k}_y = \sqrt{\bar{k}^2 + k_x^2} \tag{43}$$

always giving a real wavenumber and radiation into the plate.

3.2. Input and transfer dynamic stiffness'

With the establishment of the wavenumbers it is now possible to find the transfer functions for line excitation of a strip. This is achieved by matching the boundary conditions. If the boundary is fixed at $y = l_y$, Eq. (37a) yields a reflection coefficient $\hat{r} = -1$, and becomes

$$u(x, y) = A\{\exp(-\mathrm{i}\hat{k}_y y) - \hat{\alpha}_y^2 \exp(\mathrm{i}\hat{k}_y y)\} \exp(-\mathrm{i}k_x x). \tag{44}$$

At $y = 0$ the displacement is $U_0 \exp(-\mathrm{i}k_x x)$, therefore substitution into Eq. (44) gives

$$A = \frac{U_0}{1 - \hat{\alpha}_y^2}, \tag{45}$$

thereby describing the general wavefield. The forces F or dynamic stiffness' at position y, can be found from the Hooke's Law relationship

$$F = -S_{sy} \frac{\partial u}{\partial y}, \tag{46}$$

where S_{sy} is the side-wall shear stiffness/length on the plane normal to the y direction. If this is applied to Eqs. (44), (45), then the force F_0 at the line input, and the transmitted force F_T is given from Eq. (46)

$$F_0 = -S_{sy} \left\{ \frac{\partial u}{\partial y} \right\}_{y=0}, \quad F_T = -S_{sy} \left\{ \frac{\partial u}{\partial y} \right\}_{y=l_y}. \tag{47a,b}$$

This yields the input dynamic stiffness K_0, and the transfer dynamic stiffness K_T

$$\frac{F_0}{U_0} = K_0 = \mathrm{i}\hat{k}_y S_{sy} \frac{1 + \hat{\alpha}_y^2}{1 - \hat{\alpha}_y^2}, \quad \frac{F_T}{U_0} = K_T = 2\mathrm{i}\hat{k}_y S_{sy} \frac{\hat{\alpha}_y}{1 - \hat{\alpha}_y^2}. \tag{48a,b}$$

These are plotted in Figs. 10 and 11 for the side-wall data in Table 1. The dynamic stiffness' are shown for four different excitation wavenumbers to demonstrate above and below coincidence behaviour described in Section 3.1.

For frequencies less than 100 Hz the wavelength in the y direction is too long for travelling waves or standing waves, the behaviour is of a simple stiffness irrespective of the excitation wavenumber. Above this frequency there is the possibility of propagating waves if the excitation wavenumber k_x is less than the free shear wavenumber k_s.

If the excitation wavenumber ratio k_x/k_s is zero, Eq. (48a,b) correspond to the expressions for normal boundary excitation of a plate or end excited rod. When the wavenumber ratio k_x/k_s is 0.5 the result is similar to the zero angle case, with wave propagation and the resonant behaviour seen

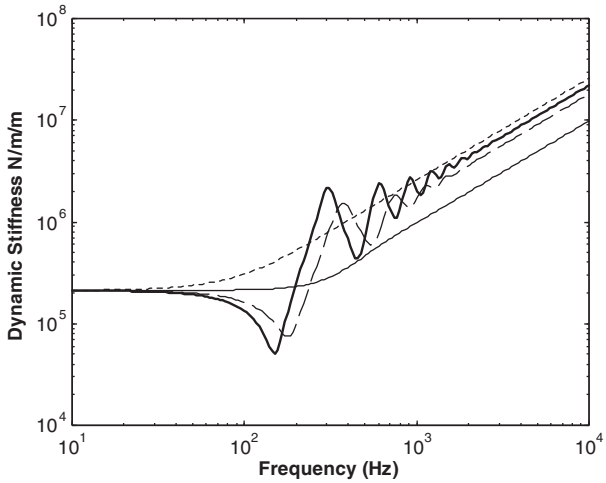

Fig. 10. Input shear stiffness modulus of an edge excited strip, varying excitation wavenumber k_x, free wavenumber k_s : k_x/k_s: —— 0.5, ––– 0.7, - - - 1.0, — 1.4.

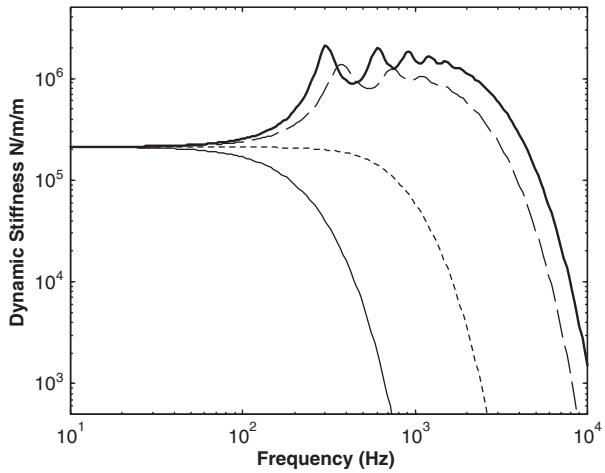

Fig. 11. Transfer shear stiffness modulus of an edge excited strip, varying excitation wavenumber k_x, free wavenumber k_s : k_x/k_s: —— 0.5, ––– 0.7, - - - 1.0, — 1.4.

in Figs. 10 and 11. The only difference is that the real part of the wavenumber $\hat{k}_y$, is reduced in accordance with Eq. (38) and the attenuation is increased in accordance with Eq. (40). This trend is seen by comparison to the $k_x/k_s = 0.7$ case in the figures, where the natural frequencies are raised and the attenuation increased for both input and transfer stiffness'.

At the coincidence condition $k_x/k_s = 1$, there is no propagating wave into the plate as the angle of incidence is zero. Therefore no resonant behaviour is seen in the input or transfer responses, and almost no force is transferred above the low-frequency stiffness region. Similar behaviour is seen when $k_x/k_s > 1$, a further increase in wavenumber ratio causes more attenuation.

From the above discussion it appears that there is some scope in force transmission control by using the side-wall and belt wavenumbers.

3.3. Modification of the vertical side-wall stiffness for the belt wavenumber

The procedure for modifying the vertical side-wall stiffness is the same as with the shear case above, except that now three wavenumbers, seen in Fig. 2a, must be modified by the belt wavenumber k_x, in Eq. (38a).

The belt wavenumber k_x is the dominant travelling transverse wave of the belt. This wave is selected from the belt dispersion curve in Ref. [3] and is displayed in Fig. 2a along with the three original side-wall wavenumbers $\bar{k}_1, \bar{k}_2, \bar{k}_3$. From inspection of this figure it is seen that the belt wavenumber is only greater than the lowest root, for the longitudinal wave. Application of Eq. (38a) therefore filters out this longitudinal wave. The effect of this filtering is seen in Fig. 12, in which the original stiffness', in Fig. 3, is plotted against the new stiffness' obtained from the modified roots.

At frequencies below 200 Hz there is no change, as the static stiffness does not involve travelling waves. At higher frequencies there is a substantial reduction in stiffness and hence transmitted force, as only the contribution from the transverse wave remains after the high impedance longitudinal waves are no longer excited.

The side-wall stiffness has been described in terms of the side-wall properties and the dominant belt wavenumber. As this belt wave is travelling in the frame of reference of the rotating tyre the resulting side-wall stiffness' should be independent of the tyre rotation speed.

The analysis so far assumes that the side-wall width is precisely the same over the whole circumference. In fact there will be a slight fluctuation in width about a mean value. The effect of this fluctuation is modelled by averaging nine transfer functions. Fig. 12 shows the effect of a 0.3% standard deviation in the plate strip width l_s. For this 100 mm side-wall, the standard

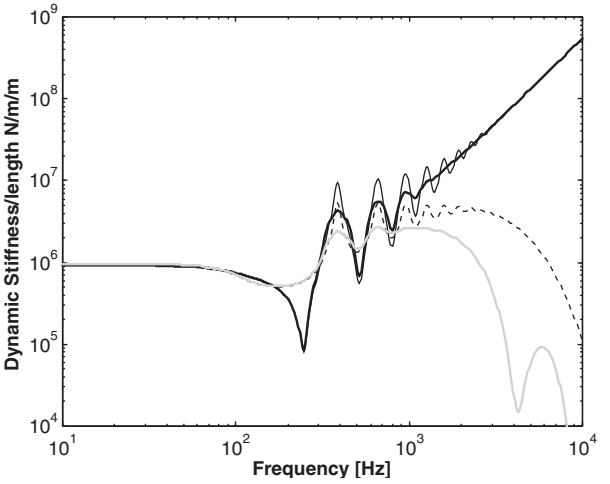

Fig. 12. Side-wall vertical stiffness modulus; modified for plate wavenumber: — input, - - - transfer, —— input 0.3% error, —— transfer 0.3% error.

deviation of the width was therefore 0.03 mm. It is interesting to see that the effect of the width fluctuation has a similar effect as an increase in damping. A realistic side-wall model can therefore be made without using particularly high damping values.

4. The force transmitted to the hub of a loaded tyre

Fig. 13 shows a loaded tyre of belt radius a and a contact patch of length l_{ct}, where $l_{ct} = 2\theta_{ct}a$. The total force transmitted in the vertical direction F_s is the sum of three components

$$F_s = F_{ct} + F_b + F_a. \tag{49}$$

F_a is the force transmitted by the 'free acoustic wave' in the cavity, and is calculated in Appendix A.1. $F_{ct} = 2K_r l_{ct} w(0)$ is the force transmitted through the side-wall at the contact patch. The force from the vibration of the unloaded belt F_b is an integral over the free belt length l_b, weighted by $\cos\theta$

$$F_b = -(2K_r + K_a)a \int_{\theta_{ct}}^{2(\pi-\theta_{ct})} w(c)\cos\theta\,\mathrm{d}\theta + 2K_c a \int_{\theta_{ct}}^{2(\pi-\theta_{ct})} u(c)\sin\theta\,\mathrm{d}\theta, \tag{50}$$

where K_r and K_c are the side-wall stiffness' in the radial and circumferential directions. The term K_a is the stiffness of the air in the cavity and is calculated in Appendix A.2. The associated belt deflections are w, u. The term containing the circumferential stiffness and deflections will be neglected here as being less than the radial term. The radial displacement is given in Eq. (36), [3], as the sum of six wave amplitudes $\mathbf{w}_p$

$$w(c) = \{1\ 1\ 1\ 1\ 1\ 1\}\mathbf{L}_{pc}\mathbf{w}_p,$$

where

$$\mathbf{L}_{pc} = \mathrm{diag}[\exp(-\mathrm{i}k_{pa}c) \quad \alpha_{pb}\exp(\mathrm{i}k_{pb}c)\cdots]_{p=1,2,3} \tag{51}$$

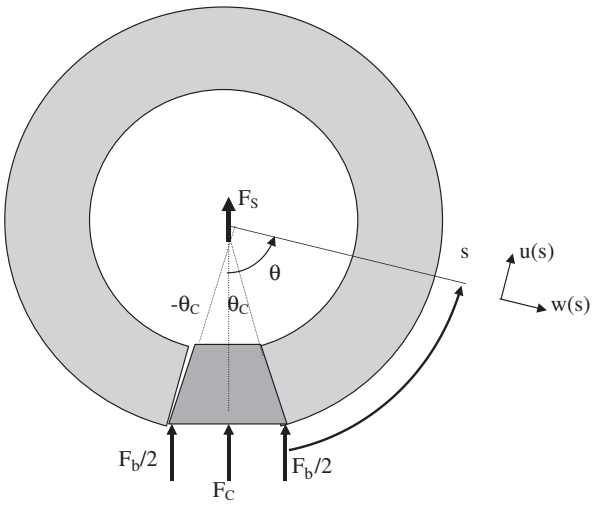

Fig. 13. Net force transmission to the hub due to a displacement on the contact patch.

and

$$\alpha_{pb} = \exp(-\mathrm{i}k_{pb}l_b),$$

where the unloaded tyre length $l_b = 2(\pi - \theta_c)$. k_{pa}, k_{pc} are the wavenumbers in the anti-clockwise and clockwise directions for the pth wavetype. The integral I_p for the clockwise or anti-clockwise terms is the same, i.e.

$$I_p = \int_0^{l_b} \exp(-\mathrm{i}k_{pa}c)\cos\,\theta\,\mathrm{d}\theta \quad \text{or} \quad \int_0^{l_b} \alpha_{pb}\,\exp(\mathrm{i}k_{pb}c)\cos\,\theta\,\mathrm{d}\theta \tag{52}$$

becoming for each wave

$$I_p = \frac{-1}{1-(k_p a)^2}\{\alpha_p(\sin\,\theta_{\mathrm{ct}} + \mathrm{i}k_p a\cos\,\theta_{\mathrm{ct}}) + (\sin\,\theta_{\mathrm{ct}} - \mathrm{i}k_p a\,\cos\,\theta_{\mathrm{ct}})\}, \tag{53}$$

where the subscript $p = pa = pb$. For the case of line excitation, $\theta_{\mathrm{ct}} = 0$, and Eq. (53) reduces to

$$I_p = \frac{1}{1-(k_p a^2)}\{\mathrm{i}k_p a(1-\alpha_p)\}. \tag{54}$$

This spacial filter mainly selects the $p = 1$ mode (rigid body translation), and the evanescent and complex waves that exist near the input. The force from the unloaded belt is therefore given from Eq. (50) and (53) as

$$F_b = (2K_r + K_a)a\sum_{p=1}^{6} I_p w_p \tag{55}$$

a sum of the six waves. The amplitude of these waves depends on the boundary conditions [1]. The total force from the contact patch and the free belt can now be found from Eq. (49).

5. Comparison of the model with measurements on a stationary tyre

Some tests were made on a smooth pressurised tyre to make comparison with the results from the belt model in Ref. [3] and the side-wall model presented here. The main purpose of the comparison is to see if it reproduces the physical phenomena observed on the tyre. Fitting of the measurements to the model will give an estimate of the mean material properties of the cross-section. Three types of test were made; the first uses a line excitation to select only the zero-order waves on the belt, the second test uses point excitation on the belt, the third test attempts to measure the force transmitted to the hub from excitation on the belt.

Measurements were made for all the transfer functions described above and the parameters of the model were varied until a reasonable fit was made to the transfer functions with a single data set. This final parameter choice used in all the predictions is given in Tables 2 and 3.

5.1. The test arrangement

Fig. 14 shows a schematic diagram of a test arrangement on a pressurised tyre on a hub bolted horizontally to a steel block weighing 200 kg. This type of mounting is needed for measurements

Table 2
Side-wall parameters from measured data

Parameters	Symbol	Size equation	Units
Internal pressure	P	2×10^5	N/m^2
Side-wall thickness	t_s	0.85×10^{-2}	m
Side-wall length	l_s	0.1	m
Side-wall angle	ϕ_s	0.68	rad
Contact angle	ϕ_1	0.36	rad
Tensile force/width	N_s	$P \times a_s$	N/m
Shear modulus	G_s	2.5×10^6	N/m^2
Shear stiffness/width	S_s	$G_s \times t_s$	N/m
Bending stiffness/width	B_s	$G_s \times t_s^3/4$	Nm
Axial stiffness/width	A_s	4.5×10^6	N/m
Belt mass/area	μ_s	9.35	kg/m^2
Rotational inertia/width	I_s	$\mu_s \times \mu_s^2/12$	kg
In-plane shear loss factor	η_{sz}	0.2	
Transverse, bending shear loss factor	η_z	0.1	
Tension loss factor	η_{tz}	0.04	

Table 3
Belt parameters from measured data

Parameters	Symbol		Size equation		Units
Internal pressure	P		2×10^5		N/m^2
Belt thickness	t		1.6×10^{-2}		m
Belt outer radius	a		0.3		m
Cavity inner radius	a_h		0.18		m
Belt width	b		0.18		m
Tensile force/width	N_c	N_z	Eq. A.4 [3]	$P \times l_s/2\theta_s$	N/m
Shear moduli	G_c	G_z	3×10^7	2×10^7	N/m^2
Shear stiffness/width	S_c	S_z	$G_c \times t$	$G_z \times t$	N/m
Bending stiffness/width	B_c	B_z	90	90	N/m
Axial stiffness/width	A_c		1.8×10^6	∞	N/m
Belt mass/area	μ		20		kg/m^2
Rotational inertia/width	I_c	I_z	$\mu \times t^2/3$	$\mu \times t^2/3$	kg
Bending and shear loss factor	η_c	η_z	0.1	0.1	
Acoustic loss factor	η_a		0.04		
Axial loss factor	η_c		0.2		
Tension loss factor	η_{tc}	η_{tz}	0.04	0.04	

of transmitted force. The excitation was band-limited white noise from an electro-dynamic exciter. For most tests the loading was applied on a line across the belt, designed to preferentially excite the one-dimensional, $m = 0$, belt waves. This load spreader was made of plywood of 0.01 m width, and was glued to the belt. The mass, including the belt section directly beneath, was 0.095 kg. The

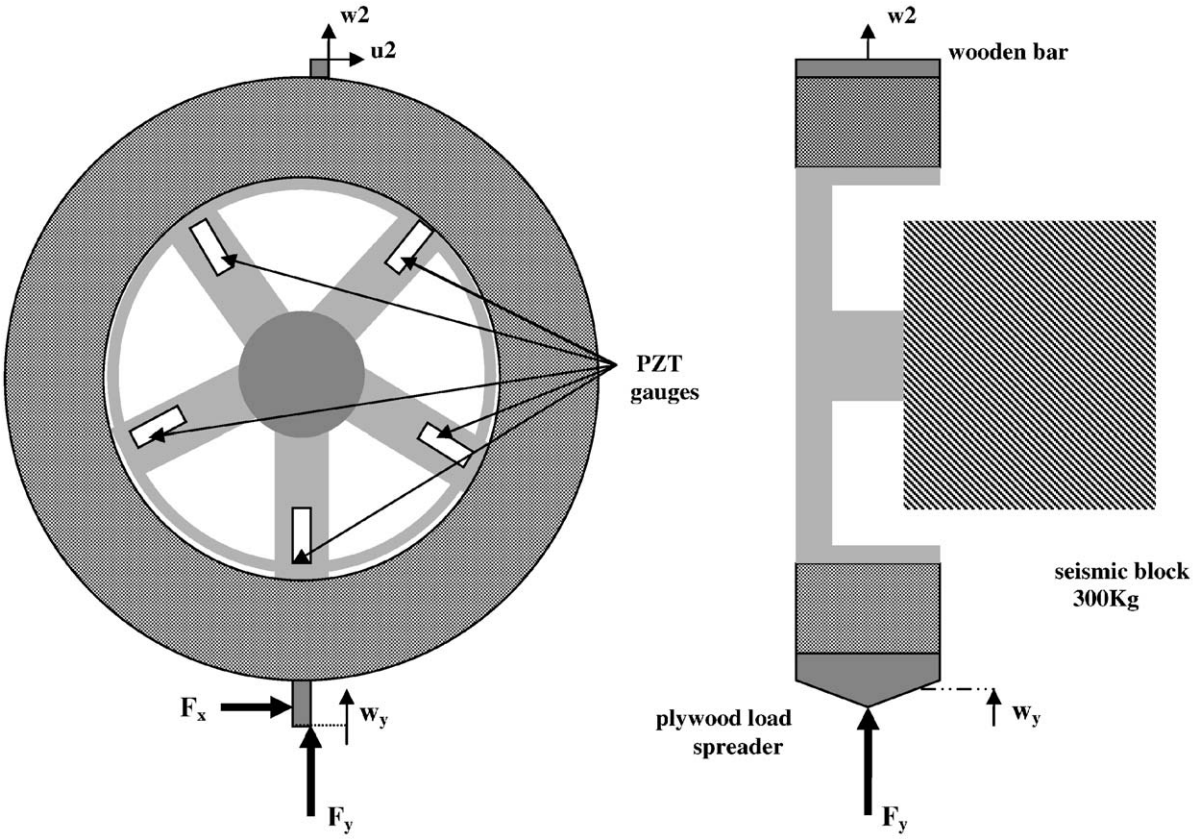

Fig. 14. Schematic arrangement for tyre tests.

load spreader exhibited a resonance at 8 kHz, below which the measured data can be assumed to be associated with a mass-less line loading. The input force and acceleration were measured with piezo-electric transducers attached to the load spreader. The transfer mobilities were measured to the diametrically opposite position at 180°, by attaching the accelerometer to a wooden square section rod glued across the belt width. This arrangement selects the $m = 0$ waves, also the increased area over that of a point measurement permits the use of a heavier and more sensitive accelerometer than could be used otherwise.

In-plane excitation was also used to measure the in-plane input line mobility. This was done by gluing the load spreader tangentially to the belt with an additional 0.1 m plywood rod attached to provide access for the exciter. This arrangement does not give a force directly in line with the belt neutral axis, as would be the case for the theoretical predictions, but rather the more realistic case of a tangential force on the belt surface offset from the neutral axis.

The force transmitted to the hub was measured using a novel means, with 5 piezo-electric chips operating as strain gauges, one glued axially to each of the radial hub elements. The idea was to locate these as close as possible to the neutral axis for bending, thereby to be only sensitive to radial in-plane forces. If the extraneous bending and shear forces are neglected the total force F_s,

transmitted in the displayed test arrangement is

$$F_s = F_1 + (F_2 + F_5)\cos\frac{2\pi}{5} + (F_3 + F_4)\cos\frac{4\pi}{5}, \tag{56}$$

where F_1 to F_5 are the forces taken in an anti-clockwise sense from the excitation position. In a calibration it was found that when a force F_y was applied externally, 95% was transmitted by F_1, 4% by $F_2 + F_5$, 1% by $F_3 + F_4$. Although the cosine weighting reduces the contribution from normal and shear forces other than F_1, it would still appear that even in a more sophisticated arrangement the force F_1 would remain dominant.

5.2. Radial and tangential line mobilities

These tests were designed to confirm the one-dimensional curved belt model. To select only the one-dimensional waves the load spreaders described above were used for radial and also tangential excitation.

The input line mobilities for radial excitation are compared in Fig. 15. At 80 Hz the belt rigid body translation mode, $n = 1$, occurs. Below this frequency the tyre resists the line force as a stiffness element. The measurement exhibits a resonance at 20 Hz, which is probably the rig resonating laterally on the contact with the floor. Between 90 and 300 Hz translation belt modes are seen. At the lower-frequency end the stiffness is from the belt tension and side-wall stiffness, both dependent on the air-pressure. At the upper-frequency end the belt bending stiffness tends to dominate. The fit between the theory and measurement is quite good both in level and frequency.

At higher frequencies, from 300 Hz to 1 kHz the fit is not so good with an overestimate of a factor of 1.5 at worst. The problem may be with the measurement, as the slope is greater than (frequency)$^{-1/2}$ which is the expected value of an infinite beam in flexure. It is possible that the load spreader is rocking slightly in this region and exhibiting a resonance around 1 kHz. Above

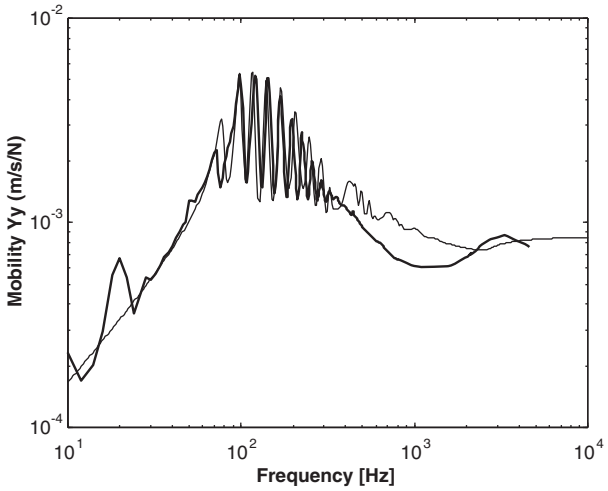

Fig. 15. Measured and predicted radial line input mobility modulus: —— measured, — predicted.

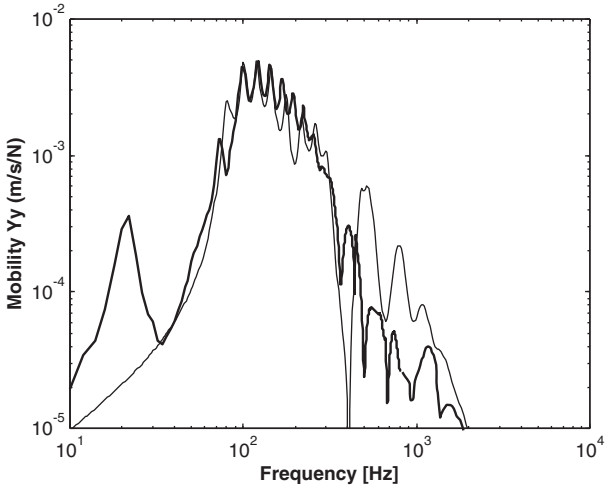

Fig. 16. Measured and predicted radial line transfer mobility modulus: —— measured, — predicted.

1 kHz the line from the theory becomes constant indicating stiffness controlled behaviour, which was fitted to the levelling off in the measured curve.

Fig. 16 shows the comparison of the radial transfer measurements made at 180°. Below 400 Hz there is a reasonable fit of the model to the measured data, as with the input measurement discussed above. Above 400 Hz the major troughs at 350, 700 Hz and 1 kHz are predicted quite well. These are the peaks in side-wall dynamic stiffness seen in Fig. 12. At these frequencies the side-wall acts as a dynamic absorber on the belt, preventing transmission around the circumference. The troughs in the side-wall stiffness in Fig. 12 will prohibit transmission to the hub at 250, 500 and 750 Hz but give no attenuation to waves travelling around the belt.

Inspection of the measured data also shows troughs at the intermediate frequencies of the predictions, where maxima were expected. This is probably because the tyre is excited slightly asymmetrically causing additional excitation to the belt rigid body transverse rocking waves, this second mode group will cause attenuation at the extra set of anti-resonant troughs. This may also explain why the predictions are overestimating by a factor of 3 in this region, although this will also related to the underestimate at the input which was discussed above. This hypothesis is supported by the single-point tests later. Figs. 15 and 16 suggest that both the belt and side-wall models are giving a fair description of the physical behaviour for belt radial motion.

Fig. 17 displays the tangential input line mobility from the measurement in comparison with the prediction. At 50 Hz the belt rigid body rotation mode occurs, followed at 80 Hz by the rigid body translation mode. The general trend then falls off to a dip at 180 Hz associated with the belt ring frequency. This is lower than is usual for a tyre, indicating that this particular tyre is not very stiff in the circumferential direction. The small peaks due to the transverse belt modes are also seen superimposed on the general trend. Above 300 Hz the agreement in the trend deteriorates slightly and the prediction underestimates the measurement. The reason for this is almost certainly because the force is offset from the belt neutral axis giving an additional rotational excitation to

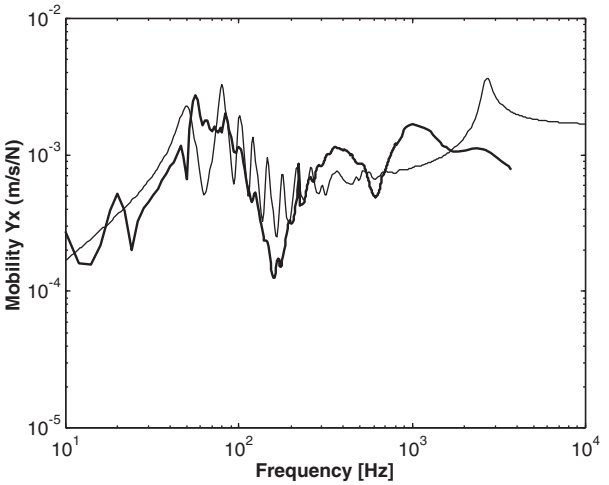

Fig. 17. Measured and predicted tangential line input mobility modulus: —— measured, — predicted.

the belt translation waves. There is a resonance near 1 kHz as was suspected from the translation measurements discussed previously. Despite these differences the prediction is nevertheless seen to describe the correct overall behaviour.

5.3. Input and transfer mobility for point excitation

The belt was driven via a 1 in diameter aluminium disc. The disc diameter d limits the shortest wavelength λ that can be driven into the belt according to: $\lambda > 2d$, and accordingly the upper cross-belt mode order. In this case only waves with cross-belt mode order $m \leqslant 7$ are included in the model for comparison with the measurement. The excitation and response were set at $b/10$ from the centre line so that all the modes would be excited.

Fig. 18 shows a comparison of the measured and predicted point input mobility. Below 300 Hz the response is dominated by the $m = 0$ waves that have been discussed above. At 330 Hz the lowest symmetric mode $m = 1$, cuts on. An attempt has been made to fit the model to this. The model then shows a second peak at 450 Hz from a side-wall mode, which does not appear in the measurement. This suggests that the simple method of modelling the higher-order modes of the section is not accurate, which was expected. The questionable assumption that the side-wall can be modelled independently from the belt at all frequencies, as at the belt cut-on frequencies, is clearly not correct. However on average, the agreement is quite good, indicating that overall the model is acceptable, with problems only occurring at the cut-on of the low-order cross-belt modes.

The transfer mobility at 180° is displayed in Fig. 19. The comparisons for frequencies of the peaks and troughs are quite good over the whole frequency range. As troughs above 300 Hz are side-wall anti-resonances it can be concluded that the side-wall model must be representing the low-frequency tension behaviour accurately. The predicted levels are not accurate, but the average is near the measurement, which must be regarded as quite impressive for such a complex and heavily damped structure.

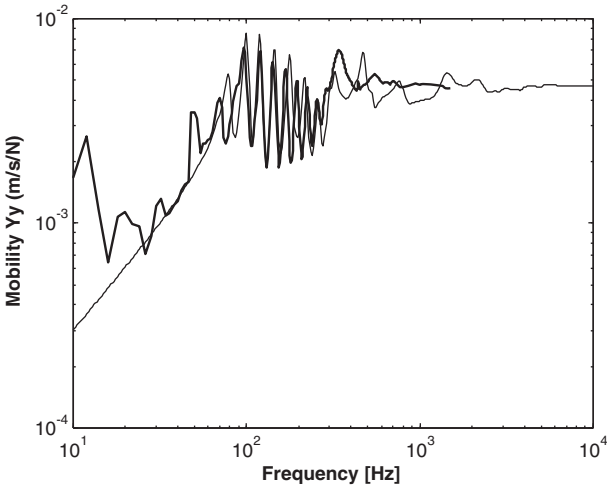

Fig. 18. Measured and predicted radial point input mobility modulus: —— measured, — predicted.

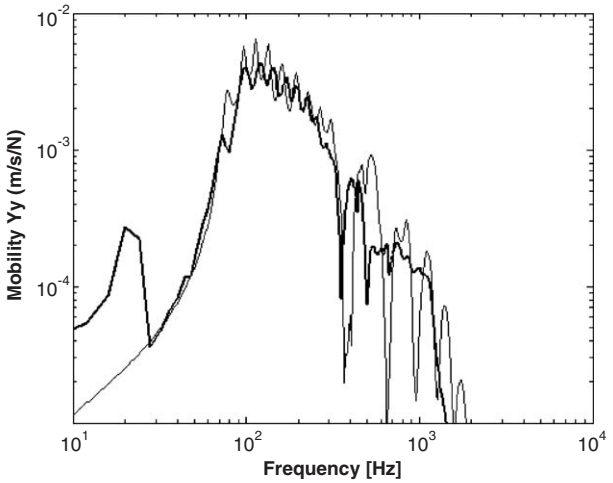

Fig. 19. Measured and predicted radial point input mobility modulus at 180°: —— measured, — predicted.

5.4. The force transmitted to the hub

The tyre model presented here only includes the air indirectly, in controlling the belt and sidewall tension. This is a good simplification for tyre surface vibration predictions, as confirmed from the good fit between theory and experiment above. However, if the requirement is for force transmission to the hub this model is no longer complete as the air in the cavity causes enhanced transmission at three frequencies in the sensitive region for interior noise below 500 Hz.

This is investigated in Appendix A, by considering the cavity pressures generated by the surface velocity, and ignoring the acoustic loading on the tyre surface. The most important of these effects

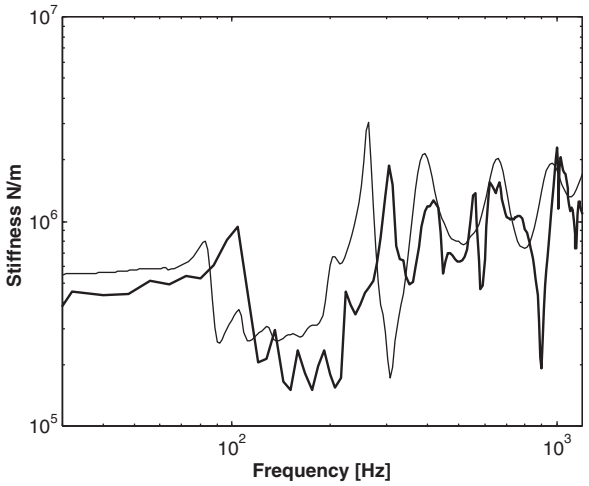

Fig. 20. Measured and predicted hub force/input displacement: —— measured, — predicted.

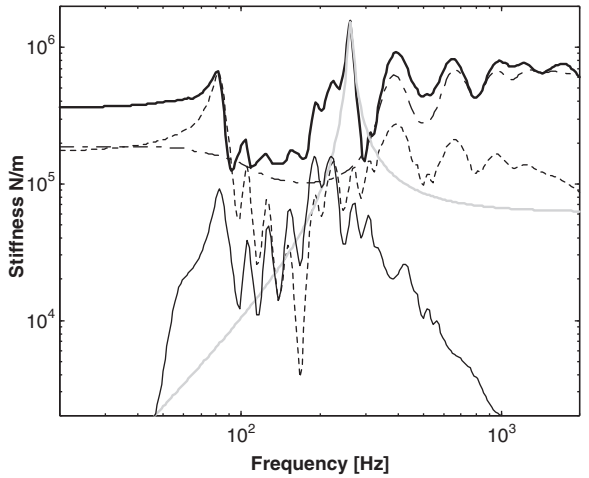

Fig. 21. Components of the hub force/input displacement: —— total, ·-·-·-·-· contact zone, - - - free belt, —— free acoustic wave, — forced acoustic wave.

is the $n = 1$ acoustic cavity mode occurring when an acoustic wavelength fits around the cavity. However the $n = 1$, belt flexural mode and the $n = 0$ ring mode have longer wavelengths than the acoustic wave and therefore transmit forces to the hub via the stiffness of the entrapped air.

Some tests were made of the theoretical predictions for transmitted force via the two side-wall components in Eq. (49), and the three structural/acoustic modes from Appendix A. The belt in Fig. 14 was excited by 0.2 m line force along the centre line. The displacement directly above the edge of the side-wall was obtained from the acceleration, and the force transmitted to the hub was measured using the piezo-electric transducers. The force/displacement or 'dynamic stiffness' was thereby obtained and are compared with the theoretical prediction in Fig. 20. Fig. 21 gives the

four components of the theoretical prediction, which will be discussed before considering the measurements. The contact length in Fig. 21 was taken as 0.1 m as this is more realistic for typical tyre.

(i) The largest single component is the force which is transmitted directly through the 0.2 m of the contact zone. It has a stiffness characteristic dependent upon side-wall curvature and tension until 200 Hz after which it is responsible for all the features above 400 Hz. This model is rather crude in that the side-wall is assumed uniform and the tapering section is neglected. However, the good fit with these measurements, and those on the belt, suggests that the influence of tension, which is not greatly influenced by the taper, is dominant. The side-wall in the contact zone supports most of the static load. The actual static stiffness will be approximately $2K_r l_{ct}$, where l_{ct} is the contact length. The contact length is not calculated here, but will be included in a later paper.

(ii) The next most important feature is the resonance around 230 Hz from the $n = 1$ acoustic wave ('free acoustic wave'). The calculation is made in Appendix A, where it is shown that the excitation is mainly from the cavity cross-section deformation in the contact zone. The remainder of the tyre carcass is assumed to be an inextensible rigid boundary. This mechanism makes no other significant contribution.

(iii) The vibration of the 'free belt' outside the contact contributes the $n = 1$ structural mode at about 80 Hz, and other belt resonance frequencies below 150 Hz.

(iv) The 'forced acoustic wave', also calculated in Appendix A, represents the transmission to the hub when the carcass motion is forced upon the air cavity. This only makes a significant contribution when the carcass wavelength approaches that of the contained air. This happens at two frequencies the $n = 1$ belt mode near 80 Hz and the belt ring frequency at about 200 Hz.

The measurements in Fig. 20 tend to confirm the predicted levels and to give a similar frequency dependence. However, complete confirmation of the model was not achieved as there is an impression that the curves are shifted by 20 Hz. The error seems to appear on the measurements, as predictions of structural frequencies are confirmed by the measurements on the belt, and the acoustic frequency is only a matter of geometry and must appear at 230 Hz. There was unfortunately a time constraint and only a single frequency response measurement taken, using random excitation between 30 Hz and 3 kHz. The statistics for the low frequencies may therefore not be reliable.

The prediction for the acoustic wave amplitude may be a little high as the tyre was only a driven on the centre line rather than over the full belt width.

6. Conclusions

A complete tyre model has been constructed and tested. The model is composed of a curved belt connected to a curved side-wall. The same wave equation is used for both components. The model is applicable between 0 Hz and the first standing wave across the belt thickness, which means it

has the capacity for both predictions of sound radiation in the 1–3 kHz region and the low-frequency vibration region below 500 Hz.

The side-wall was modelled here as the circular arc of variable angle which could be rotated to give a variable angle of connection with the belt. Both parameters have quite a large influence on the side-wall and belt tension. The side-wall model does not describe the bending well as the thickness is assumed uniform, however in the lower frequency region this is not important as tension dominates the response. When the side-wall is coupled to the belt, the in-plane transmission through the side-wall does not seem to occur because the waves in the belt are too slow to radiate vibration into it. The side-wall model modified to compensate for this effect gave a reasonable fit for both belt vibration and transmission to the hub.

The model presented here does not directly include the air within the cavity in the coupled equations, but this omission has little effect on the belt vibration. The effect of the air cavity was included using uncoupled acoustic equations. It was found that the free acoustic wave causes a resonance at 230 Hz, as is well known. There were also contributions from the stiffness of the air at the belt $n = 1$ mode and the ring frequency.

The response for translation and in-plane forces are modelled, for both input and transfer responses. The belt standing waves controlled the test tyre below 300 Hz; above this frequency the side-wall and infinite belt behaviour were the main influences on tyre response.

A technique to measure average tyre cross-section properties, with a line input and response, was successfully tested. Also a means to measure the force transmitted to the hub using piezo-electric chips, was tested. For a stiff symmetric hub this method could probably be used with some confidence.

The higher-order modes across the belt were modelled, but the cut-on frequencies are not accurate because of the simplicity of the assumed cross-belt mode shape. This is the greatest shortcoming in the model. However, the high-frequency response above 1 kHz and the noticeable cut-on frequencies seem to be in agreement with the measurements.

Acknowledgement

The support by the EC fifth framework program of the RATIN project is gratefully acknowledged.

Appendix A. Force transmitted to the hub via the air cavity

The tyre model includes the air in the cavity indirectly, as the pressure controls the belt and side-wall tension. However, the air is not included as an independent wave bearing medium. This omission does not influence the belt vibration but it affects the force transmission to the hub in two ways. First the $n = 1$ cavity mode, which causes an audible tone around 250 Hz within the passenger compartment, is neglected. The second is the stiffening of the belt due to cavity volumetric changes. Both of these effects are calculated here by considering the 'free' and 'forced' acoustic waves in the cavity, but an initial stage calculates the change in section area δA due to belt radial displacement w.

Consider the tyre section of area A and inextensible side-wall of length l_s seen in Fig. 22. The sum of the two end segments has an area A_1

$$A_1 = a_s^2(2\phi_s - \sin 2\phi_s). \tag{A.1}$$

The central rectangle has area $A_2 = w_s b$. The side-wall radius and height are

$$a_s = \frac{l_s}{2\phi_s}, \quad w_s = l_s \frac{\sin \phi_s}{\phi_s}. \tag{A.2a,b}$$

The total area is

$$A = A_1 + A_2. \tag{A.3}$$

The fractional change in area arising from a belt displacement w is

$$\frac{\mathrm{d}A}{\mathrm{d}w} = \frac{\mathrm{d}A_1}{\mathrm{d}\phi_s} \cdot \frac{\mathrm{d}\phi_s}{\mathrm{d}w} + b, \tag{A.4}$$

where

$$\frac{\mathrm{d}A_1}{\mathrm{d}\phi_s} = \frac{l_s^2}{2\phi_s^2}\left(\frac{\sin 2\phi_s}{\phi_s} - 1 - \cos 2\phi_s\right), \quad \frac{\mathrm{d}w}{\mathrm{d}\phi_s} = \frac{l_s}{\phi_s^2}(\phi_s \cos \phi_s - \sin \phi_s).$$

The general case of coupling between the carcass and the enclosed air, is obtained from the wave equation of the enclosed air excited by the change in cross-section δA, calculated above. The tyre is assumed to be inextensible, only the shape of the section controls the enclosed air volume.

Fig. 23a shows an element of length δc of the tyre cavity, where the increase in volume δV is given in terms of the belt displacement w and air axial displacement u_a as

$$\delta V = w \cdot \frac{\mathrm{d}A}{\mathrm{d}w} \cdot \delta c + A \frac{\partial u_a}{\partial c} \cdot \delta c. \tag{A.5}$$

This is related to the dynamic pressure p_a by the static pressure P and adiabatic gas constant γ as

$$p_a = -\gamma P \frac{\delta V}{A \cdot \delta c}. \tag{A.6}$$

The equation for horizontal equilibrium of force in the cavity is

$$\rho \ddot{u}_a = -\frac{\partial p_a}{\partial c}, \tag{A.7}$$

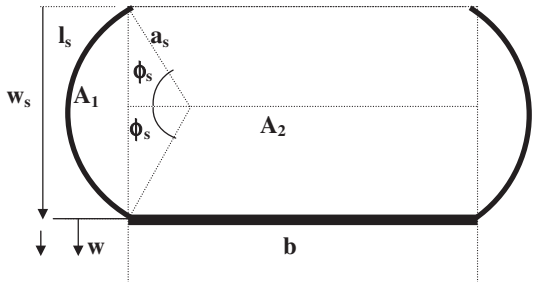

Fig. 22. Tyre cross-section.

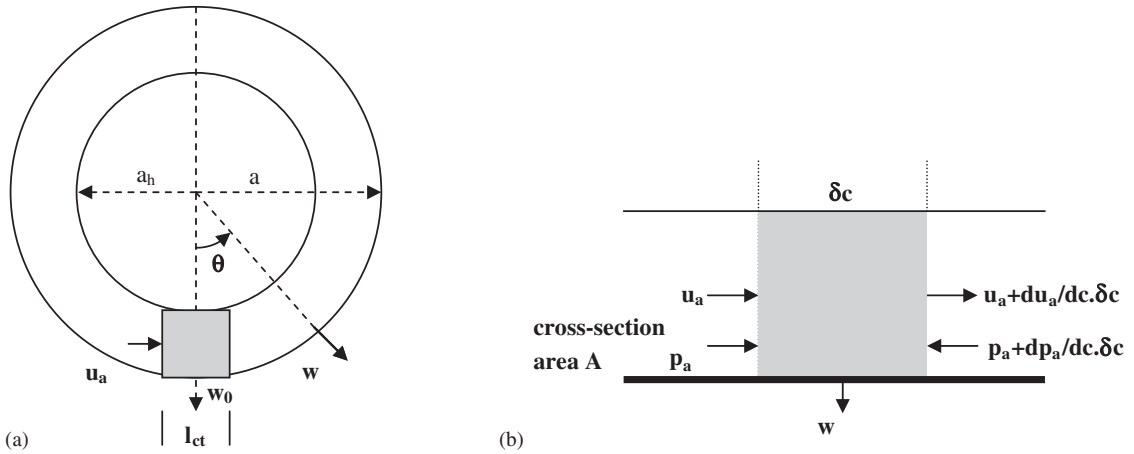

Fig. 23. Air cavity elements: (a) general case and (b) at the contact patch.

where ρ is the air density. The equation of motion is obtained by combining Eqs. (A.5–A.7)

$$\frac{\partial w}{\partial c}\cdot\frac{\mathrm{d}A}{A\mathrm{d}w}=-\frac{\partial^2 u_a}{\partial c^2}+\frac{\rho\ddot{u}_a}{\gamma P}. \tag{A.8}$$

The forcing function due to volumetric change is on the left while the dynamic response of the air is on the right.

A.1. The force transmitted to the hub from the contact patch

The solution to the wave equation is the sum of the forced and free solutions. The free solution calculated here is obtained by setting the forcing function to zero, i.e.

$$0=\frac{\partial^2 u_a}{\partial c^2}+k_a^2 u_a, \tag{A.9}$$

where the acoustic wavenumber k_a is defined as

$$k_a^2=\omega^2\frac{\gamma P}{\rho}.$$

Within the air cavity, seen in Fig. 23a, the solution to Eq. (A.9) takes the form

$$u_a=u_{aa}\exp(-\mathrm{i}k_a c)+u_{ab}\exp(\mathrm{i}k_a c), \tag{A.10}$$

where u_{aa} and u_{ab}, are the amplitudes of the anti-clockwise and clockwise waves at the contact at $\theta=0$. The circumferential distance for the acoustic wave is $c=a_a\theta$. The radius for the acoustic wave a_a lies between the belt radius a, and the hub radius a_h. The wave amplitudes are found from the two boundary conditions. The first is that symmetry may be invoked to give $u_a=0$ at $c=a_a\pi$. Eq. (A.10) gives

$$u_{ab}=-u_{aa}\alpha^2,\quad \alpha=\exp(-\mathrm{i}k_a a_a\pi), \tag{A.11}$$

where α is the attenuation and phase change of the wave travelling half a circumference; α^2 is the change over a complete circumference. At the contact where the belt displacement is w_0 the acoustic displacement u_{a0} is given from volume conservation of the air in the shaded zone seen in Fig. 23a

$$u_{a0} = w_0 \frac{l_{\mathrm{ct}}}{2A} \frac{\mathrm{d}A}{\mathrm{d}w}, \tag{A.12}$$

where l_{ct} is the length of the contact, and the other terms are from Eqs. (A.1)–(A.5). At the contact where $c = 0, u_a = u_{a0}$, therefore

$$u_a = \frac{u_{a0}}{1 - \alpha^2}. \tag{A.13}$$

The acoustic displacement at any point c becomes

$$u_a = \frac{u_{a0}}{1 - \alpha^2} (\exp(-\mathrm{i}k_a c) + \alpha^2 \exp(\mathrm{i}k_a c)). \tag{A.14}$$

The acoustic pressure is then found by using

$$p_a = -\gamma P \frac{\partial u_a}{\partial c} \tag{A.15}$$

which on making the substitution from Eq. (A.15) gives

$$\frac{p_a}{u_{a0}} = \frac{\mathrm{i}\gamma P k_a}{1 - \alpha^2} (\exp(-\mathrm{i}k_a c) + \alpha^2 \exp(\mathrm{i}k_a c)). \tag{A.16}$$

The net force towards the hub is the weighted integral of the pressure around the cavity, which after substitution from Eq. (A.12) becomes

$$\frac{F_a}{w_0} = \frac{\mathrm{i}\gamma P k_a a b l_{\mathrm{ct}}}{1 - \alpha^2} \frac{\mathrm{dA}}{A \mathrm{d}w} . I,$$

$$I = \int_0^{\pi} (\exp(-\mathrm{i}k_a c) + \alpha^2 \exp(\mathrm{i}k_a c)) \cos\theta \, \mathrm{d}\theta. \tag{A.17}$$

The integral I becomes

$$I = \frac{\mathrm{i}k_a a_a (1 - \alpha^2)}{1 - (k_a a_a)^2}. \tag{A.18}$$

Therefore, the net force to the hub from the acoustic wave is

$$\frac{F_a}{w_0} = -l_{\mathrm{ct}} b \frac{\mathrm{dA}}{A \, \mathrm{d}w} \frac{\gamma P (k_a a_a)^2}{1 - (k_a a_a)^2}. \tag{A.19}$$

The main feature is a single peak when $k_a a_a = 1$, the frequency at which there is a single acoustic wavelength in the cavity. Acoustic damping within the cavity will give k_{a0} an imaginary component that will control this peak level.

A.2. The force transmission by the acoustic wave forced by the belt

The other component of the transmitted force is caused by the action of the free belt waves on the acoustic space. This effect is calculated from Eq. (A.8) by considering the forced solution of acoustic displacement u_a and pressure p_a to the excitation function from the belt, seen on the left-hand side. The belt radial displacement is composed of three pairs of waves $p = 1, 2, 3$ of amplitude w_p and wavenumbers k_p. The belt waves and associated forced acoustic waves have the form

$$w = \sum_{1}^{3} w_p \exp(\mp \mathrm{i} k_p c), \quad u_a = \sum_{1}^{3} u_{ap}(\mp \mathrm{i} k_p c), \quad p_a = \sum_{1}^{3} p_{ap}(\mp \mathrm{i} k_p c). \tag{A.20}$$

Eq. (A.8) becomes

$$\pm \mathrm{i} k_p w_p \frac{\mathrm{d}A}{A \mathrm{d}w} = u_{ap}(k_a^2 - k_p^2). \tag{A.21}$$

By substitution from Eq. (A.15) the acoustic pressure for the pth clockwise or anticlockwise wave is

$$p_{ap} = -\frac{\omega^2 \rho}{k_a^2 - k_p^2} \frac{\mathrm{d}A}{A \mathrm{d}w} w_p. \tag{A.22}$$

The stiffness/length of the air K_a that acts on the belt and the hub is the product of the pressure and the belt width b

$$K_a = \frac{p_{ap} b}{w_p} = \frac{\omega^2 \rho b}{k_a^2 - k_p^2} \frac{\mathrm{d}A}{A \mathrm{d}w}. \tag{A.23}$$

This can be added to the side-wall radial stiffness $2K_r$ in Eq. (50) to give the total force transmission to the hub. It can be seen that only the long wavelengths, when $k_a > k_p$, associated with the belt in-plane motion will give stiffness coupling. These waves are only important at the belt $n = 1$ mode and the ring frequency, when $n = 0$.

References

[1] G. Mastinu, S. Gaiazzi, F. Montanaro, F. Pirola, A semi-analytical model for steady-and transient-state simulations: tyre models for vehicle dynamic analysis, *Vehicle System Dynamics*, Vol. 27, Swets and Zeitlinger, 1997.

[2] R.J. Pinnington, Radial force transmission to the hub from an unloaded stationary tyre, *Journal of Sound and Vibration* 253 (5) (2002) 961–983.

[3] R.J. Pinnington, A wave model of a circular tyre. Part 1: belt modelling, *Journal of Sound and Vibration*; doi:10.1016/j.jsv.2005.03.023.